First Demonstration of Airborne SAR Tomography Using Multibaseline L-Band Data

Andreas Reigber and Alberto Moreira, *Senior Member, IEEE*

***Abstract*—In synthetic aperture radar (SAR) interferometry, the phase differences between two different sensor positions are used to estimate the terrain topography. Although it is possible in this way to find a three-dimensional (3-D) surface representation, the distribution of the different scatterers in the height direction at a fixed range and azimuth position remains unknown. Contrary to this, tomographic techniques enable a real geometric resolution capability in the height direction and introduce new possibilities for many applications and inversion problems. Even misinterpretations in SAR images caused by layover and foreshortening effects can be solved by the tomographic processing.**

In this paper, the successful experimental realization of polarimetric airborne SAR tomography is demonstrated for the first time. We present the concept of aperture synthesis for tomographic imaging for the case of a multibaseline imaging geometry and discuss the constraints arising from the limited number of flight tracks. We propose a method for reduction of the height ambiguities associated to the irregular and undersampled spatial distribution of the imaging positions. Finally, we address the experimental requirements for polarimetric airborne SAR tomography and show experimental results using a multibaseline data set acquired in L-band by DLR's experimental SAR (E-SAR) of a test-site near Oberpfaffenhofen, Germany.

***Index Terms*—Ambiguity suppression, polarimetry and interferometry, SAR processing, synthetic aperture radar (SAR), three-dimensional (3-D) imaging, tomography.**

I. Introduction

THE STANDARD product of a single-channel SAR sensor is a two-dimensional (2-D) image of the scene reflectivity with high resolution in the slant range and azimuth direction [1], [2]. This image in principal represents a projection of the three-dimensionally (3-D) distributed backscattering amplitudes onto a 2-D plane. SAR interferometry additionally performs a measurement of the terrain topography in the direction perpendicular to azimuth and to the line-of-sight by analyzing the phase differences between two images obtained from slightly different positions. These phase differences are used to determine on a pixel by pixel basis the off-nadir angle and by this, the corresponding height information. The resulting height is associated to the effective phase center of all scatterers within the resolution cell. With interferometry it is possible to generate a 3-D height surface, but the distribution of scatterers in height is underdetermined and cannot be resolved by a single baseline measurement.

Manuscript received September 29, 1999; revised April 26, 2000.

The authors are with the German Aerospace Center (DLR), Institute for Radio Frequency Technology, D-82234 Oberpfaffenhofen, Germany (e-mail: Andreas.Reigber@dlr.de).

Publisher Item Identifier S 0196-2892(00)08903-8.

Polarimetric SAR interferometry was a first step in the abatement of the scattering ambiguity problem in the height direction. By combining interferometric and polarimetric techniques, it enables the separation of different scattering mechanisms within a resolution cell and at the same time, the estimation of the associated heights. The phase decomposition performed in polarimetric SAR interferometry uses the full polarimetric data and estimates for each image pixel three orthogonal scattering mechanisms [3]–[6]. For example, for a vegetated area the three different scattering mechanisms can be described as (in a simplified model): 1) a single bounce contribution from the ground; 2) a double bounce contribution from the trunks; and 3) a diffuse (volume) contribution from the tree leaves and branches. However, it is not possible with this technique to separate the contributions of the same scattering mechanism distributed over different heights.

Tomography is a well known technique in several scientific fields as well as an established tool in medical applications. Computer-aided X-ray tomography (CT) and nuclear magnetic resonance tomography (NMR) are widely used in the medical field. In the first case a narrow X-ray beam is transmitted for a set of angle positions 360° around the object [7]. As depicted in Fig. 1, the attenuation occurred by passing the object is measured by a set of sensors positioned at opposite side to the transmitters. For each angle position the received signal corresponds to a projection of the object attenuation in the transmitting direction. The projection-slice theorem [8] postulates that the Fourier transform of the received signal corresponds to a slice of the 2-D Fourier transform of the attenuation function for a given angle position. The CT processing consists of performing first a one-dimensional (1-D) FFT, which leads to a 2-D representation of the attenuation distribution in a polar format. Next a interpolation step from polar to Cartesian format is performed. Finally, a 2-D inverse FFT leads to the final image, which gives the 2-D object attenuation map at each position.

It has been shown in several papers [9]–[11] that the spotlight SAR azimuth processing can be formulated in a similar way to the CT technique. Also, the azimuth SAR processing in stripmap mode is analogous to the described tomographic processing. Due to the small angle variation associated with the SAR processing, it was possible to develop very effective algorithms that avoid the 2-D interpolation step [12]–[18]. The formation of the synthetic aperture in SAR generally has to be considered as a tomographic technique.

The main issue in this paper is achieving a real 3-D imaging with a 2-D SAR. In the case of the X-ray tomography, the third imaging dimension is not achieved by tomographic principles at all. Instead, the same 2-D processing is repeated in several po-

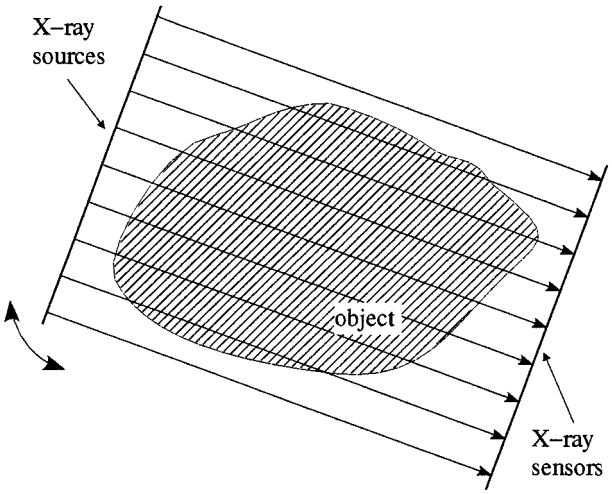

Fig. 1. Imaging geometry for computer-aided X-ray tomography. Transmitter and receiver positions are rotated around the object.

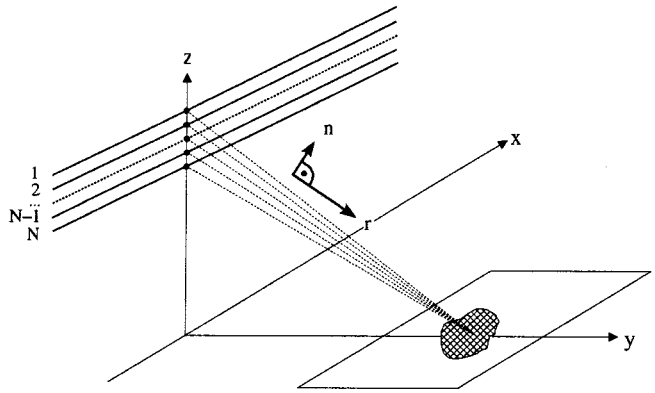

Fig. 2. Multibaseline imaging geometry for tomographic SAR. Synthetic aperture in azimuth (flight path) provides a high azimuth resolution (x-direction), and the aperture in z-direction allows a geometric resolution in height.

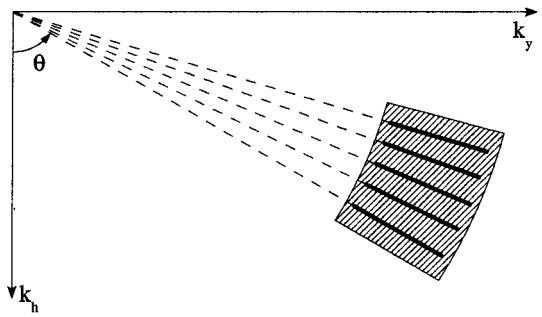

Fig. 3. Spectral representation of multibaseline SAR images. The SAR illumination with different off-nadir angles reconstructs a 2-D part of the reflectivity spectrum in the range-height frequency domain. Tomographic processing then can achieve a spatial resolution in the height direction.

sitions across the object, i.e. by carrying out in small steps parallel translations of the transmitter and receiver set. This translational operation as by the CT technique cannot be applied here due to the wide elevation beam of a SAR system and the variety of objects which have to be imaged. The basic idea is therefore to form a second synthetic aperture in the direction of the translational movement (see Fig. 2). This direction, denoted as normal direction $\vec{n}$, is perpendicular to the line-of-sight (range or across-track) $\vec{r}$ and azimuth (flight) directions $\vec{x}$.

Assuming a fixed azimuth position x_o, the received SAR signal $s(t)$ under a given off-nadir angle θ is a convolution of the complex reflectivity $a(y, h)$ with the transmitted signal $p(t)$, where h denotes the height and y the ground range coordinates. Therefore, its spectrum can be expressed in terms of the Fourier transforms of the signal $P(\omega)$ and the reflectivity $A(k_y, k_h)$

$$\begin{aligned} S(\omega) &= P(\omega)A(k_y, k_h) \\ &\text{with } k_y = \frac{2\omega}{c}\sin\theta \\ k_h &= \frac{2\omega}{c}\cos\theta \end{aligned} \tag{1}$$

whereas ω is denoting the radar angular frequency and c the speed of light.

In Fig. 3, this situation is illustrated in the wavenumber domain, i.e., in the range and height frequency domain.[1] We see that the spectra of images acquired from different positions (i.e., with different off-nadir angles θ) contain different slices of the spectrum of the reflectivity $A(k_y, k_h)$. By using a series of flight tracks, we can derive in this way a knowledge about a 2-D area of the reflectivity spectrum. By tomographic processing of these data, the spatial reflectivity function $a(y, h)$ can be reconstructed.

In order to obtain several slices of the reflectivity spectrum, various imaging geometries are possible. For the case of airborne SAR, these are especially circular [19] and multibaseline [20] flight paths, whereas the latter is the technique adopted in our experiment. Fig. 2 depicts the imaging geometry with the synthetic aperture in azimuth and height directions.

We introduce the following definitions, which have not been clearly defined in the SAR literature so far.

1) *Tomographic SAR*: System configurations forming an additional synthetic aperture in the normal direction. The synthetic aperture in azimuth direction is associated with a variation of the so-called squint angle, while the synthetic aperture in the normal direction is associated with a variation of the off-nadir angle for each object. It can also be interpreted as a multibaseline interferometry with the number of tracks being much greater than two.
2) *3-D SAR*: System configuration using a circular flight path around the object, i.e., the imaging capabilities are primarily associated to a variation of the squint angle and not the off-nadir angle. For example, the object located in the focal point of the circular path has no off-nadir angle variation, and it is not possible to solve for this object the scattering contributions at different heights as by SAR tomography.
3) *Interferometric SAR*: System configurations consisting of two tracks (or two antennas) that measure the topography of the terrain. The height associated with the topography

[1]In SAR processing, the wavenumber ($w - k$) domain is often related to the range and azimuth (Doppler) frequency domain.

is related to the position of the phase center of all backscattering contributions within each resolution cell.

The basic idea of radar tomography has already been mentioned in the literature [20]–[22], but until now, experiments have only been done under laboratory conditions [23], [24] or in the spaceborne case with limited imaging capabilities [25], [26]. This paper is concerned with the first practical demonstration of airborne SAR tomography using high resolution polarimetric L-band data. In Section II, we review the basic SAR tomographic processing formulation. We propose a processing procedure for the image formation that accounts for the motion compensation step required in the airborne case. Further we present a new procedure for suppressing the ambiguities which arises from the irregular distance intervals between the tracks. Simulation results are presented to demonstrate the efficiency of the proposed approaches. In Section III, the imaging results obtained with 14 parallel tracks over the test site of Oberpfaffenhofen over Germany, acquired with the E-SAR system of DLR [27] are presented and discussed. Section IV concludes the paper, giving some suggestions for further research work.

II. Multibaseline Tomographic SAR Processing

A. Basic Principle

The basic principle of tomographic SAR focusing is to perform an aperture synthesis in the n-direction out of the different flight tracks. As the distances between the tracks can stay small for a reasonable resolution in height, we do not follow the direct wavenumber-domain reconstruction. Instead, a more efficient approach using only one FFT is made. The necessary processing steps for this and the occurring signal properties can be explained best by using first a simplified geometry.

As shown in Fig. 4, we assume in the following equally spaced baselines and neglect all projections related to the off-nadir angle θ, i.e., $\vec{n}$ is considered to have the same direction as $\vec{z}\,(\theta = 90°)$. In the real side-looking case, d would correspond to the baseline perpendicular to the line-of-sight, and n to a height of $h = n\sin(\theta)$. The path length (two-way) between the sensor at position z and a scattering element at height n_0 and a minimum range distance of r_0 can be expressed as

$$r(z, n_0) = 2\sqrt{r_0^2 + (z - n_0)^2} \simeq 2r_0 + \frac{(z - n_0)^2}{r_0} \qquad (2)$$

and the received signal s_r can be modeled as

$$s_r(z, n_0) = a(r_0, n_0) * \exp\left(-\frac{ik}{r_0}(z - n_0)^2\right) \qquad (3)$$

where $a(r_0, n_0)$ denotes the complex reflectivity in the distance r_0 at height n_0 and k the wavenumber $2\pi\lambda$. The received signal consists of the complex reflectivity convolved with a quadratic phase function. This chirp signal is a function of the z-direction and has a zero frequency offset if $n_0 = 0$. It shows positive frequency offsets if the height of the target is positive (see Fig. 5). s_r is similar to the signal of a burst mode SAR like ScanSAR [28]. In the ScanSAR case, the Doppler centroid is varying according to the target azimuth position.

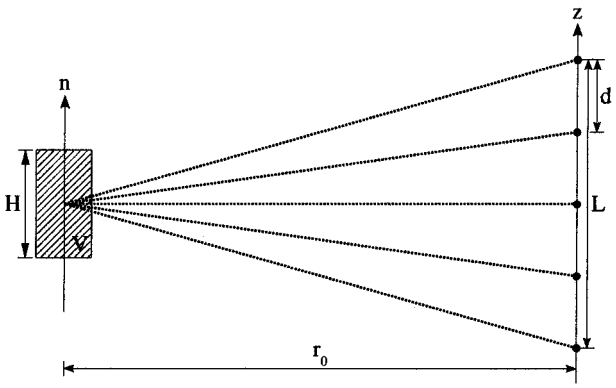

Fig. 4. Simplified tomographic imaging geometry ($\vec{z} = \vec{n}$). The SAR sensor illuminates a volume V at different positions on the z-axis. The total height of the volume is H, the baseline between the several illumination positions is d, and the maximum length of the tomographic illumination path is L.

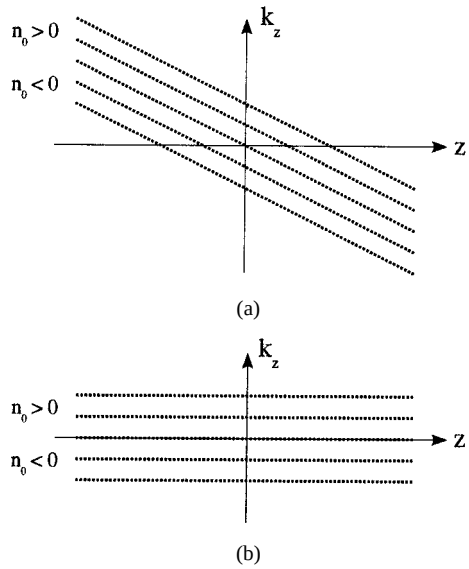

Fig. 5. Frequency dependency of the tomographic signal in the z–k_z-plane (height/height frequency domain) for different scatterer positions. (a) Received tomographic signal s_r and (b) tomographic signal after deramping s_d.

For processing ScanSAR data, which is already range compressed, the so-called spectral analysis (SPECAN) algorithm has been widely adopted [29] and will be used in a slightly modified version for the tomographic processing proposed in this paper.

The SPECAN algorithm has two basic assumptions. The first approximation is related to the approximation made in (2), i.e. the received signal has a quadratic phase modulation. The second assumption is that the range migration is very small, i.e. the variation of $r(z)$ for $-L/2 < z < +L/2$ is smaller than half the slant range resolution cell. In our simulations and image processing with real SAR data, we have corrected the phase variation without any approximation and performed the range cell migration correction exactly. In the following, however, we keep these two approximations for better understanding of the tomographic imaging mechanism and properties.

The first step in the SPECAN algorithm is to compensate the quadratic phase variation by multiplying the received signal s_r by a complex conjugate quadratic phase function. This oper-

ation is denoted as deramping and is illustrated in Fig. 5. By multiplying the received signal with a deramping function

$$u(z) = \exp\left(+\frac{ik}{r_0}z^2\right) \tag{4}$$

a demodulated signal s_d can be obtained

$$s_d(z, n_0) = a(r_0, n_0) * \exp\left(-\frac{ik}{r_0}\left(n_0^2 - 2zn_0\right)\right). \tag{5}$$

The spatial frequency k_z of deramped signal s_d is no longer dependent on the z-position [see Fig. 5(b)]. It depends only on the height n_0 of the occurring scattering processes

$$k_z(n_0) = \frac{\partial \arg(s_d)}{\partial z} = \frac{2kn_0}{r_0}. \tag{6}$$

The final step in the SPECAN algorithm is to perform a spectral analysis by means of a fast Fourier transform (FFT). According to (6), the k_z-domain (height frequency domain) is equivalent to the spatial n-domain. The desired image result $v(n, n_0)$, therefore, is equal to the Fourier transform of the deramped signal in the z-direction $S_d(k_z, n_0)$

$$\begin{aligned} v(n, n_0) &= S_d(k_z, n_0) \\ &= a(r_0, n_0)\, e^{-(ik/r_0)n_0^2} \int_{-L/2}^{L/2} \exp\left(\frac{2ik}{r_0}(n_0 - n)z\right) \mathrm{d}z \\ &= a(r_0, n_0) \cdot L \cdot e^{-(ik/r_0)n_0^2} \cdot \mathrm{sinc}\left(\frac{kL}{r_0}(n_0 - n)\right) \end{aligned} \tag{7}$$

where $\mathrm{sinc}(x)$ stands for the $\sin(x)/x-$function. From the width of the sinc-function, the geometric resolution in the z-direction results as

$$\delta_z = \frac{\lambda r_0}{2L}. \tag{8}$$

For example, a L-band SAR system with 5000 m range distance r_0 achieves a height resolution of approximately 2 m, with a tomographic illumination path L of 300 m. Furthermore, it is important that the illumination path is properly sampled in order to avoid height ambiguities. This means that the sampling distance d must be sufficiently small to fulfill the Nyquist criterion for the spatial bandwidth of s_d. If this cannot be fulfilled, high sidelobes and ambiguities will occur in the image, as in the case of azimuth ambiguities for 2-D SAR imaging. The sampling distance d, which is necessary for unambiguous imaging, depends on the total height H of the examined volume

$$d \leq 1/B_{s_d} = \left|-2\pi\left(\frac{\partial \arg(s_d)}{\partial z}\right)^{-1}\right| = \frac{\lambda r_0}{2H}. \tag{9}$$

In our example, a maximum baseline separation of ≈20 m has to be held for a volume height of 30 m. The total number of required tracks of 15 is obtained by dividing the illumination path of 300 m by the baseline separation of 20 m. Increasing the volume height to 60 m means to decrease the baseline separation to 10 m and to increase the number of tracks to 30 if the height resolution of 2 m is to be kept.

Interestingly, (7) contains a phase term proportional to n_0^2. This term corrupts the image phase, which should ideally be independent from the position of the target. For simple imaging, where only the amplitudes are of interest, this is irrelevant. But for polarimetric and other applications that require a phase-preserving image reconstruction, it is necessary to remove this term by multiplying an inverse phase term after the final image has been generated. A similar multiplicative step is necessary in the SPECAN approach to achieve phase preserving processing [14].

B. Airborne Case

However, under realistic conditions, it is not possible to obtain equally spaced baselines, and the real tracks show deviations from the nominal positions in both the y- and z-directions. Because of practical constraints, we are also limited to a relatively small amount of flown tracks. The result is that our synthetic aperture in the n-direction is always unevenly sampled, and even worse, in some parts normally strongly undersampled with respect to the examined volume height (i.e. the condition of (9) is violated).

The first step in processing real SAR data obtained from N different tracks is to correct the data samples for a constant slant-range distance. This can be achieved by replacing the deramping function of (4) by a phase correction term of the form

$$u_i = \exp(ik(r_i - \langle r\rangle)) \tag{10}$$

where

r_i denotes the range distance between the ith sensor position $\vec{p}_i$ and a reference point in the middle of the focus;
$\langle r\rangle$ $1/N \sum_i r_i$.

After this phase correction, the data samples appear like they have been acquired from positions on a reference circular arc around the reference point as depicted in Fig. 6. This step is similar to the line-of-sight phase correction in stripmap SAR motion compensation. The ith data sample now has a form similar to (5)

$$s_i(n_0) = a(r_0, n_0) * \exp\left(-\frac{ik}{\langle r\rangle}\left(n_0^2 - 2l_i n_0\right)\right) \tag{11}$$

where l_i denotes the ith distance along the l-direction (Fig. 6). Analogous to (7), a focusing can be achieved by transforming the deramped signal to the k_l-domain corresponding to the spatial n-domain. k_l, denoting the wavenumber in the l-direction, can be derived as in (6)

$$\begin{aligned} v(n, n_0) &= 1/N \sum_{i=1}^{N} s_i \exp(-ik_l l_i) \\ &= 1/N \sum_{i=1}^{N} s_i \exp\left(\frac{2ik}{\langle r\rangle} n l_i\right). \end{aligned} \tag{12}$$

The shape of the resulting impulse response now depends on the distribution of the sensor positions and cannot be described in an easy way. Due to the uneven sampling of the aperture, the result is always a disturbed response that does not show a main ambiguity in the distance $\Delta n = \lambda r_0/2d$ but a generally increased ambiguity level starting next to the main lobe. A closer sampling would reduce the ambiguity problems, but with a limited

number of tracks for a practical realization it will also deteriorate the n-resolution.

If the Nyquist criterion is fulfilled for all data samples, a resampling operation to a regular sampling along the n-direction followed by spectral analysis (FFT-operation) will lead to the same sinc-function as in the previous section (7). In practice however, this is not the case and the resampling operation with undersampled data strongly deteriorates the image quality. This problem will be assessed in the next section and a solution will be proposed and validated with simulated data.

C. Ambiguity Suppression

As is well known in azimuth SAR imagery, the ambiguity level caused by undersampling is one limiting factor for the image quality in the azimuth direction. In the azimuth SAR case, an ambiguity suppression greater than ≈25 dB is required for achieving high image quality. This value is obtained by selecting a sufficiently high PRF for a given imaging mode. This PRF value ensures the correct sampling of the Doppler bandwidth, while the azimuth antenna diagram suppresses the ambiguous higher Doppler frequencies. In the tomographic case, the elevation antenna diagram is very wide, leading to the different properties when compared with the azimuth SAR case

1) The ambiguities are not suppressed by the elevation antenna diagram for the entire swath width. The height ambiguities therefore appear periodically in intervals of $\lambda r_0/2d$. This means that the total height H of the examined layer cannot go beyond this limit. In our example in Section II.B, the ambiguity height separation of 30 m is achieved for a baseline separation of $d = 20$ m. This constraint defines the tomographic geometry for a given application.
2) In a practical case (air- and spaceborne), it will not be possible to hold a constant baseline separation for all tracks. Additionally, very possibly the distance between some tracks will violate the maximum allowed baseline separation. This irregularity increases the sidelobes of the tomographic impulse response and deteriorates the height ambiguity ratio.

The first item mentioned previously does not necessarily imply a deterioration of the image quality if the imaged volume has a sufficient small height. Our concern here is to find a solution for the problems listed in the second point. It turns out the question how these sidelobes caused by the under- and irregular sampling can be reduced during processing of the data.

In the case of only an irregular baseline separation, the data can be transformed to a regular grid before processing by an oversampling and resampling step. But this presumes that the distances between all sampling positions are clearly below the limit given in (9). In practice, it can happen that this condition is missed for at least some intervals. Backscattering contributions far from the central position of the examined volume are associated with higher spatial frequencies. The undersampling and the resulting frequency aliasing of these components prevents a proper interpolation of the data.

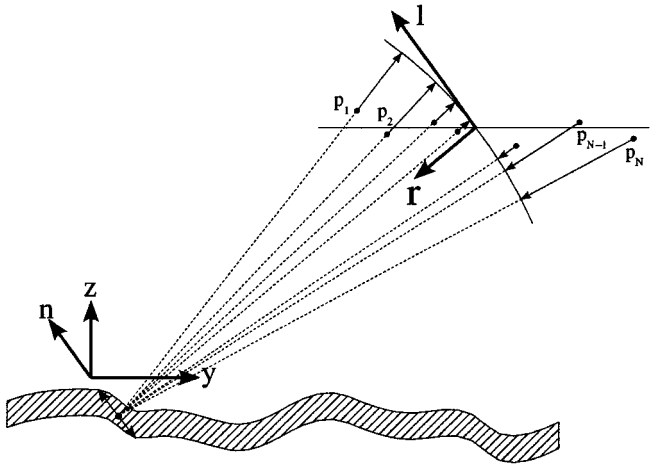

Fig. 6. Deramping operation of a tomographic data set obtained from non-ideal positions p_i as a result of unevenly distributed flight tracks. This operation is precisely performed by applying a phase correction proportional to the distances between the real positions p_i and an ideal (circular) imaging geometry around a reference point in the middle of the focus. The l-direction is parallel to the n-direction.

To find a remedy for this problem, the integer interferogram combination technique [35], [36] can be applied to fill up the longer gaps of the irregular tomographic sampling. Under the simplifying assumption that a single backscattering contribution is dominant in the examined volume, the tomographic signal can be modeled by a dominant spatial frequency. In this case, s_i behaves autoregressive, and it is possible to estimate in a simple way its function values at some synthetic track positions. Under this model, the interferogram between two adjacent tracks for a scatterer at position n_0 can be written as

$$I_{i,\,i+1} = s_i s_{i+1}^* = a\,(r_0,\,n_0)^2\,\exp\!\left(-\frac{ik}{\langle r\rangle}\,(2\Delta l_{i,\,i+1} n_0)\right). \tag{13}$$

With this interferogram, it is possible to add to every sensor position l_j two new simulated tracks at the positions $l_j \pm \Delta l_{i,\,i+1}$

$$\begin{aligned} s_j^+ &= s_j * I/|I| \\ &= a\,(r_0,\,n_0)\,\exp\!\left(-\frac{ik}{\langle r\rangle}\left(n_0^2 - 2\,(l_j + \Delta l_{i,\,i+1})\,n_0\right)\right) \end{aligned} \tag{14}$$

$$\begin{aligned} s_j^- &= s_j * I^*/|I| \\ &= a\,(r_0,\,n_0)\,\exp\!\left(-\frac{ik}{\langle r\rangle}\left(n_0^2 - 2\,(l_j - \Delta l_{i,\,i+1})\,n_0\right)\right). \end{aligned} \tag{15}$$

We can see that these new synthetic signals are identical to signals that would have been received from the positions $l_j + \Delta l_{i,\,i+1}$ and $l_j - \Delta l_{i,\,i+1}$. As noted before, this is only valid under the assumption of one single dominant scatterer within the considered volume. For multiple scatterers, it can be shown (see appendix) that the newly derived signals can still be considered as a valid approximation of the real signals, as long as only track combinations with small baselines are selected in (13). To minimize errors, we used for the estimation of new signals only interferograms obtained from baselines smaller than half of the actual gap to be filled up. After the generation of the synthetic

signals, the data is still unevenly sampled, but due to the much denser sampling, which satisfies the Nyquist-criterion, an interpolation to a regular grid is now possible.

To check the applicability of this method, it was tested on a simulated data set. In Fig. 7(a), a simulated scatterer distribution $|a(r, n)|$ in the azimuth/height-plane is shown. It consists of a three-layer volume target (two of them having a random distribution) on the left side of Fig. 7(a), two separated scatterers in different heights in the middle and a single scatterer placed over the whole height range on the right side of this figure. The system parameters used in the simulation correspond to our experimental conditions, the focused volume has a height extension of $H = 40$ m. In Fig. 7(b), we see the direct tomographic processing of the described scatterer distribution by a sufficient amount of equally distributed tracks. A resolution of approximately 3 m is achieved in the height direction. Contrary to this, we observe in Fig. 7(c) that a tomographic processing using a smaller amount of nonuniformly and undersampled track positions shows a high ambiguity level, leading to a poor image contrast. The result obtained from the same data as in Fig. 7(c), but with the proposed ambiguity suppression method applied is shown in Fig. 7(d). Here, the single diagonal line of scatterers at the right side is perfectly reconstructed independently from its position in the focused height. The sidelobes were suppressed to $\approx$15 dB (no weighting was applied). But also for the distributed targets on the left side where only an approximate generation of synthetical samples is possible, we can observe a clear improvement in the quality of the reconstruction.

In addition to the Fourier transform, several other spectral estimation techniques [30] can be applied to further reduce the ambiguity problem. Especially higher order autoregressive techniques are very promising since already with the presented simple method, it is possible to achieve good results. A reduction of the ambiguity problems might also reduce the experimental effort, as a lower number of tracks would be necessary to achieve the desired image quality.

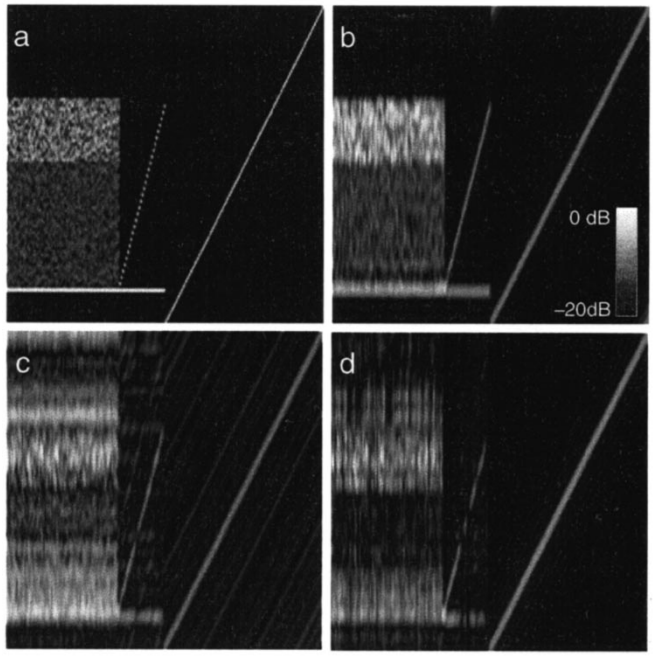

Fig. 7. Tomographic processing of simulated data. (a) Simulated scatterer distribution $|a(r, n)|$ in the azimuth(horizontal)/height(vertical)-plane, (b) reconstruction using 25 equally spaced tracks of 10 m horizontal baseline, (c) reconstruction using 14 irregular distributed tracks with an average baseline of 20 m, and (d) reconstruction using the same track configuration as in (c) and applying the proposed ambiguity suppression method

III. Experimental Results

The experimental realization of the presented concept is not a trivial task, especially not for the airborne case, where a relatively unstable sensor platform is used. But as a long wavelength with high penetration capabilities like the L- or P-band is necessary for the imaging of a volumetric scatterers, spaceborne sensors drop out from the outset because of an actual lack of these frequencies. On the other hand, airborne sensors have a much higher flexibility in the realization of special experimental needs.

As a platform, we used DLR's experimental SAR system (E-SAR). The E-SAR is a multifrequency SAR system, that operates polarimetric in X- and C-band, and fully polarimetric in L- and P-band [27]. The airplane used by the E-SAR is a small DO 228 turboprop aircraft operating at a typical height of 10 000 ft. In order to produce a tomographic image with such an airborne platform, a couple of requirements must be fulfilled. In particular, an extremely good measurement of the imaging geometry, as well as the technical equipment for the realization of a relatively complicated track configuration, are necessary. In our case, the position, velocity, and the position angles of the aircraft are recorded by a CCNS4/Aerocontrol navigation system, which uses a combination of D-GPS receivers and an LTR-81 inertial navigation system for the measurement of the platform position and position angles, respectively. The absolute position accuracy of the CCNS system is specified to 0.2 m, the relative accuracy to 0.05 m. The position angles are specified with an accuracy better than 0.03°. The CCNS system additionally gives the pilot an online feedback about the flight path during data acquisition by using a real-time D-GPS position processing with an accuracy of a few meters. This facilitates considerably the compliance of the planned flight tracks for the pilot and the deviations from the nominal setup are minimized to an acceptable level.

As discussed in Section II, a track distribution with a long distance between the furthermost tracks is needed for high z-resolution, and at the same time a small distance between adjacent tracks to avoid image ambiguities. Because of the limited amount of tracks that can be recorded during a mission it is necessary to find a good compromise here. For a first demonstration of airborne SAR-tomography a suitable L-band data set was acquired in May 1998 on the test site of Oberpfaffenhofen, Germany. During this campaign, fully polarimetric data sets with a processed spacial resolution of $\approx$ 1.0 m in azimuth and 2.3 m in range were recorded from 13 parallel flight tracks. We planned a respective distance of approximately 20 m between the tracks. For this configuration, a resolution of 2.9 m in the z-direction can be expected for midrange, the height ambiguity would be about 35 m. Additionally, we tried to repeat the first track after completion of the other 13 tracks to be able to check for eventual temporal decorrelation. To facilitate the setup for the pilot, all

tracks were specified to be flown at the same height. Of course, it was not possible to achieve the ideal planned geometry in the experiment, the real flight paths are shown in Fig. 8. Altogether approx. 300 MB of raw data have been collected per square kilometer of imaged area, considering all the 14 flight tracks.

The errors arising from the aircraft movements are compensated by a two step motion compensation during the SAR processing [31]. Additionally, a very precise velocity and range delay variation compensation have been carried out. The reference tracks for motion compensation of each track are calculated to be parallel, having the effect that, except of the known deviations due to different slant-range projections, the resulting SAR images would be already coregistered in an ideal case. Small inaccuracies in the order of few millimeters in the relative positioning within each track are leading to a residual misregistration in azimuth of the processed images with a standard deviation of about 25 cm.

The absolute positioning inaccuracy in space is larger and lies in the order of centimeters. The analysis of the echoes of several corner reflectors clarified that this error is a kind of offset which is constant over the duration of one track. To minimize the influence of this error on the tomographic processing, a calibration of the imaging geometry was performed using the position and phase of one single corner-reflector in the scene. Finally, we checked for temporal effects by forming the interferogram between the first and the last track, which have a difference in acquisition time of 3.5 h. The coherence of this interferogram shows clearly that temporal effects are negligible in our case, as the coherence even over forest exceeds the value of 0.9.

To generate the 3-D SAR image out of the acquired raw data, first normal 2-D SAR processing was performed, using an extended chirp scaling processor [14]. In the following, the resulting SAR images must be precisely coregistrated to eliminate residual mis-registrations due to uncompensated motion errors. This was done by applying a refined procedure for estimation of the misregistration followed by a resampling step of the SAR images. Then the actual tomographic processing according to Section II can be performed. It starts with the deramping step (10), followed by the synthesis of additional tracks (14) and (15). This extended data set is next resampled to a regular grid. Finally a Fourier-transform leads to the final image result. Additionally, we applied a Hamming weighting ($\alpha = 0.75$) for a better suppression of the sidelobes. One slice (azimuth line) of the result in the height/azimuth plane is shown in Fig. 10(a)–(c) for HH, VV, and HV polarization, respectively.

As it can be seen in the corresponding amplitude image Fig. 10(d), the right part of the image consists of nearly flat grass land with a corner reflector placed on it. In the middle of the image, we find a row of parked cars followed by a building (left middle). After the building, the azimuth slice crosses some bushes, a street, and then enters a dense spruce forest with a height between 15 and 20 m (see also Fig. 9).

As the result of the height ambiguity, the image contrast over the volumetric targets is reduced. On the other hand, the ambiguities of point and surface scatterers are well suppressed, and the tomographic processing shows much better results in this case. In Fig. 11 the impulse response, in the z-direction of the corner reflector is shown both with and without the proposed

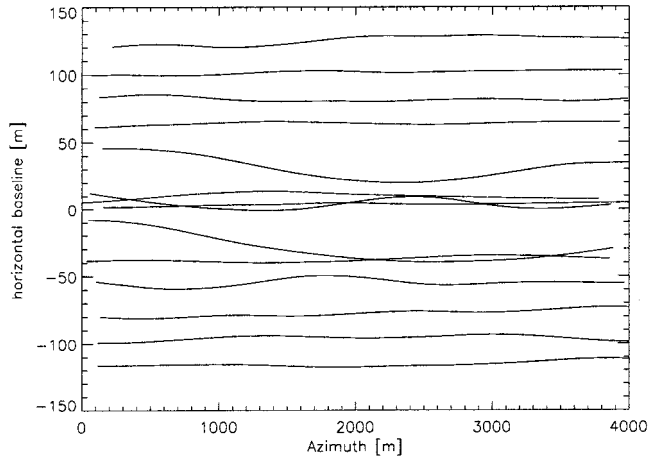

Fig. 8. Achieved horizontal baselines over azimuth during data acquisition. The nominal baseline was specified to 20 m and could only be satisfactorily fulfilled for the eight furthermost tracks (four at each side).

Fig. 9. Photo of the spruce forest. This forest type shows two dominant characteristic scattering mechanisms: double bounce scattering via ground and stems and random volume scattering in the crown.

ambiguity suppression method. We can see that after applying the ambiguity suppression method the sidelobe level is very low (< -25 dB) for this single dominant target. The 3 dB width of the main lobe is 3.1 m, which demonstrates that the theoretical resolution of 2.9 m can nearly be achieved with real tomographic data.

Some of the scene contents described earlier are visible in the tomographic slice. In the right part of the image in Fig. 10, the flat meadow appears as a nearly horizontal line. Its real topographic height is equivalent to the measured height. Slightly above the ground level, the strong echo of a corner reflector is visible in the right middle of the image. A little bit more to the left appears the roof of the building several meters above the ground level. From the difference between the height of surrounding ground level and the height of the roof the height of the building can be estimated and validated with the real one ($\approx$13 m). Of special interest is the spruce forest. Here, the crown and the underlying ground appears bright in the slices obtained in HH and VV polarization. In the cross-polar channel, only the crown is visible. This is a result of the different scattering mechanism contributions occurring in this kind of volumetric target.

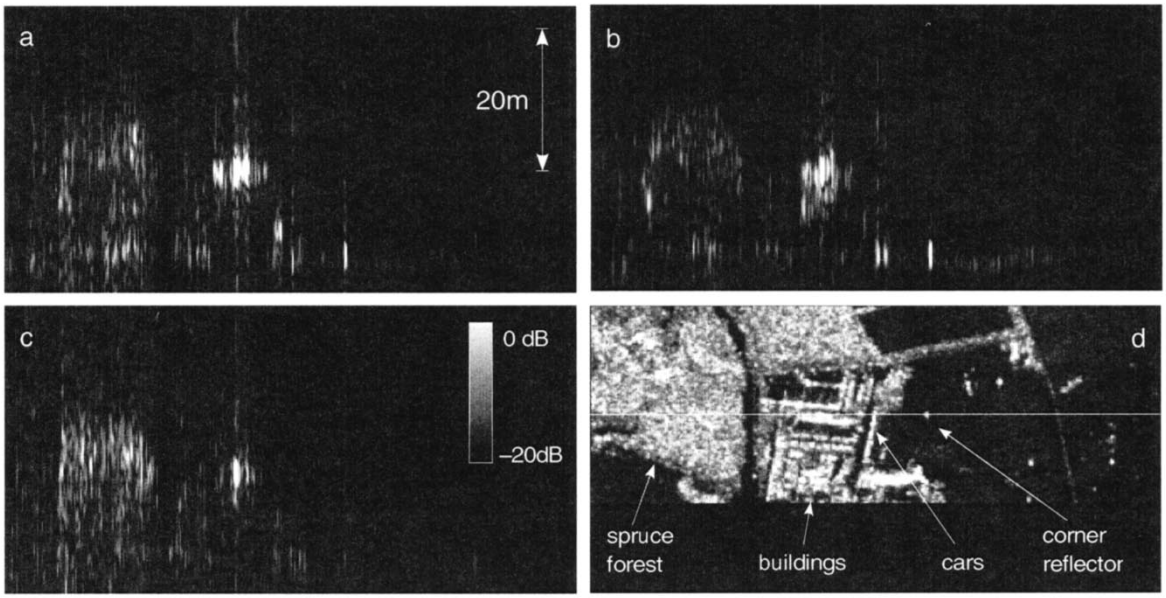

Fig. 10. Slices in the height(vertical)/azimuth(horizontal)-direction of the tomographic processing result $|v(r,\ h)|$. (a) HH-polarization, (b) VV-polarization, (c) HV-polarization, and (d) SAR amplitude image with marked position of the tomographic slice in the azimuth direction. Image dimensions are 35 m $\times$ 720 m (height $\times$ azimuth). The main sensor and processing parameters are L-Band, mean velocity 90 m/s, middle range distance 4500 m, azimuth and range resolution 1 m $\times$ 2 m, resolution in height direction 2.9 m.

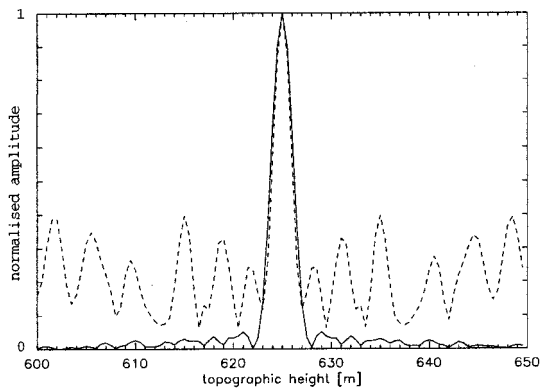

Fig. 11. Impulse response of the corner reflector. Dashed line: without ambiguity suppression, solid line: after applying the proposed ambiguity suppression method and with weighting (Hamming $\alpha = 0.75$).

1) *Double Bounce*: This backscattering contribution appears due to the double bounce scattering mechanism between the tree trunks and ground level. This contribution has its scattering phase center on the ground and is not present in the cross-polar channels.
2) *Volume Scatter*: A second backscattering contribution is observed in all channels from the randomly oriented needles in the crown. The apparently stronger contribution in the HV polarization is just caused by an amplitude dynamic adjustment carried out for optimizing the contrast of the image.

The differences in height between these two different scattering mechanisms allow us to estimate the height of the forest. Comparing the forest height visible in the tomographic slices with hypsometric ground truth measurements, [34], a good agreement between both heights can be observed.

If we compare the azimuth slices obtained in different polarizations, we can already observe several differences. But additionally to these amplitude images also the phase relations between the polarizations contain valuable information about the backscattering process. From the azimuth slices presented in Fig. 10, the polarimetric scattering matrices can be calculated. These scattering matrices are obtained in the HH/VV-basis and can be transformed to the Pauli-basis by a target decomposition [3]. The advantage of the Pauli-basis lies in the strong relationship between the elements of the polarimetric scattering matrix in this basis to three basic scattering mechanisms. The first scattering mechanism of Pauli-matrix contains the echo of isotropic odd-bounce scatterers, like flat surfaces or trihedral corner reflectors. The second is related to isotropic even-bounce scattering, especially double bounce. The third one corresponds to isotropic even-bounce scattering with an orientation rotated by $\pi 4$, normally occurring in the case of random volume scattering and on double bounce targets whose axis is rotated to the line-of-sight direction (e.g., dihedral corner reflectors with a rotation of 45°).

The result of the Pauli-decomposition is shown in Fig. 12. It demonstrates that the proposed tomographic processing with ambiguity suppression preserves the full polarimetric information present in amplitude and phase of the data. The corner reflector on the right side appears in blue coming from the triple-bounce scattering occurring here. A little bit more to the left, we find a red spot at ground level related to double-bounce scattering coming from the cars parked in this area. The roof of the building produces a mixture of odd and even bounce scattering, but have nearly no cross-polar echo except of a bright spot in the middle of the building that is strong and almost equal in all polarizations. In the spruce forest, we can now clearly identify the type of the different scattering mechanisms in the height direction. The red color of the ground level indicates that the echo

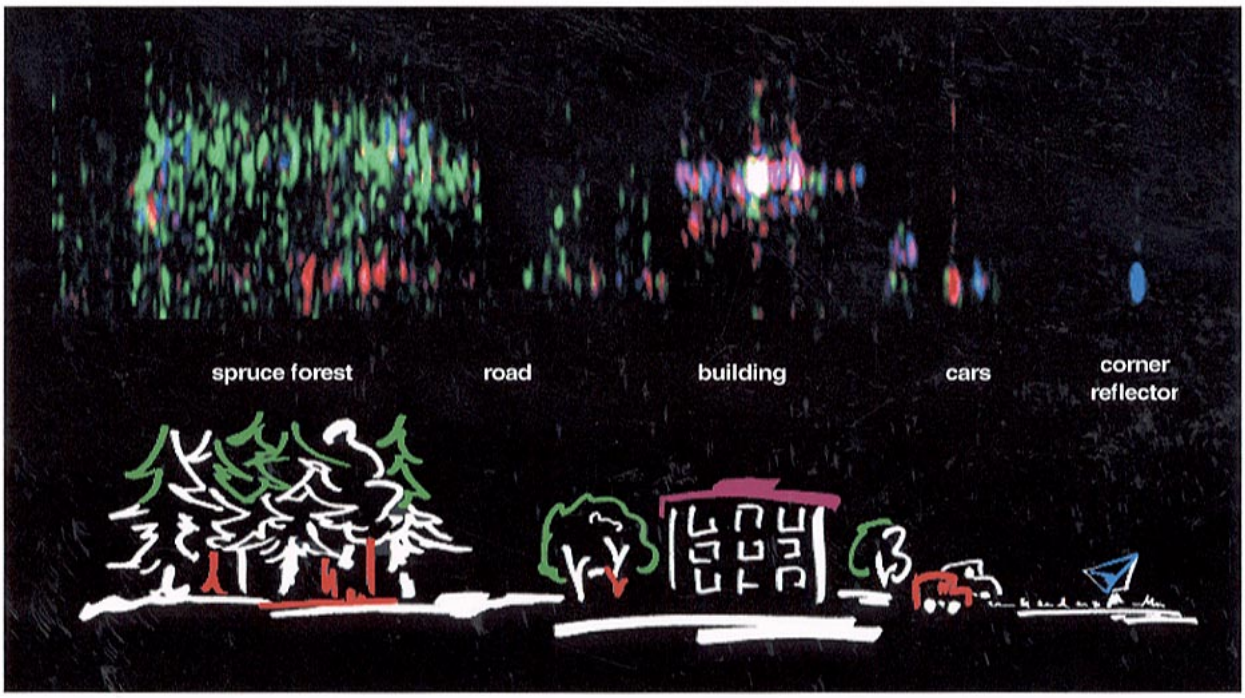

Fig. 12. Upper image: Polarimetric color composite in the {\sc Pauli}-basis of a tomographic slice in the height/azimuth-direction. (blue = HH + VV, red = HH − VV, and green = 2*HV). Lower image: Schematic representation of the imaged area.

coming from here is due to a double bounce scattering from the trunks. The crown now appears in green which is characteristic for random volume scattering.

IV. Discussions, Conclusions and Future Activities

In this paper, we have described the concept and signal properties of multibaseline SAR tomography and demonstrated the principal technical feasibility using an airborne platform. The results presented here are only a first step into a new topic that shows a great potential in respect to several applications. The inversion of geophysical parameters of a volumetric target from conventional 2-D SAR images leads in several cases to ambiguous classification results. Because several different scattering effects from different heights are mixed in the resolution cell, a reliable inversion is not always possible, even using multifrequency and polarimetric data. The capability of SAR tomography to resolve the backscattering contributions coming from different heights can be used to improve the inversion of geophysical parameters in SAR imaging. For surface and point scatterers having no height distribution, the tomographic imaging leads to the same results as conventional interferometric SAR imaging.

In the scope of future activities, the potential for many applications will be assessed like the estimation of the ground topography, the biomass, vitality, and the height of vegetated areas and also the detection and positioning of covered objects. Furthermore, SAR tomography can contribute to solve with an improved reliability several inversion problems like the estimation of the soil roughness and humidity, ice thickness and humidity, and many other classical applications requiring an image classification. Even misinterpretations in SAR images caused by layover and foreshortening effects may be solved by tomographic SAR imaging due to the capability to have a height resolution.

It must be mentioned that SAR tomography for topographic mapping is affected in a different way than in traditional SAR interferometry by the errors caused by an imprecise tilt angle value, i.e., inaccurate knowledge of the roll angle. This means that SAR tomography can also be used for accurate terrain topographic mapping. In our case, the achieved terrain height resolution was $\approx$3 m. Also, a comparative accuracy analysis between SAR interferometry and tomographic for topographic measurement will be performed in a follow-on work.

In the case of digital elevation models of forestry areas, it is normally desired to estimate the ground topography and not the top of the vegetation layer. As we have seen, even in a longer wavelength like the L-band, a significant contribution of the backscattering is occurring in the crown. Since for the traditional SAR interferometry only the total phase center of all scattering effects is relevant, the estimated height would be clearly above the ground level. With SAR tomography, it is possible to separate the ground backscattering in the forest and to estimate a height only from signal contributions related to it.

As far as the measurement of the biomass or the stem volume over forestry areas is concerned, a strong correlation between the backscattering amplitude and the present biomass has been shown in the case of conventional 2-D SAR remote sensing. However there exist the problem, that for L- and P-band a saturation is already reached for a relatively small biomass. This is due to strong backscattering contributions in the crown of the trees, which are not related to the biomass, but are still significantly strong (even in P-band). Until now, only VHF-SAR has been suitable to do reasonable measurements over forest with a density greater than 200 tons/ha [33]. On the other hand, the

VHF frequency range has the disadvantage of being inaccurate in the estimation of biomass values lower than 100 tons/ha. SAR tomography allows us to estimate the backscatter contribution of the crown and to separate it from the other scattering components. The crown contribution can be used to calculate the attenuation occurred in the crown and to correct the double-bounce contribution from the stems. In this way, it should be possible to circumvent the saturation problem in wavelengths like L- and P-band. This will be considered in our future experiments.

Further work will also include the development of improved algorithms for a better suppression of ambiguities of volume targets and optimization of the computational efficiency of the tomographic processing algorithms. Furthermore, the comparison of the results with those of longer wavelengths using the polarimetric P-Band mode of the E-SAR system will be very interesting as well as a model-based polarimetric analysis and decomposition of the tomographic images.

APPENDIX
AMBIGUITY SUPPRESSION

In case of multiple scatterers in the examined volume, the deramped signals s_1 and s_2 from two track position l_1 and $l_1 + \Delta l$ can be expressed as

$$s_1 = \sum_i \exp\left(-\kappa\left(n_i^2 - 2l_1 n_i\right)\right),$$
$$s_2 = \sum_j \exp\left(-\kappa\left(n_j^2 - 2\left(l_1 + \Delta l\right) n_j\right)\right) \tag{16}$$

where κ stands for $ik/\langle r\rangle$ and amplitudes $a(r_0, n_0)$ are assumed to be constant for simplification. The interferogram between s_1 and s_2 results as

$$I_{12} = s_1 s_2^* = s_1 \cdot \sum_j \exp\left(\kappa\left(n_j^2 - 2l_1 n_j\right)\right) \exp(-2\kappa \Delta l n_j). \tag{17}$$

From this, a new synthetic data sample at position $l_2 + \Delta l$ can be derived

$$s_3^+ = s_3 * I_{12} = \sum_k \exp\left(-\kappa\left(n_k^2 - 2l_2 n_k\right)\right) * I_{12} \tag{18}$$
$$= \sum_k \sum_j \exp\left(-\kappa\left(n_k^2 - 2l_2 n_k\right)\right) \exp(-2\kappa \Delta l n_j) \cdot \exp\left(\kappa\left(n_j^2 - 2l_1 n_j\right)\right) \cdot s_1. \tag{19}$$

Introducing $\Delta n_{jk} = n_j - n_k$, this expression can be written as

$$s_3^+ = \sum_k \sum_j \exp\left(-\kappa\left(n_k^2 - 2\left(l_2 + \Delta l\right) n_k\right)\right) \cdot \exp\left(-2\kappa \Delta l \Delta n_{jk}\right)\right) \exp\left(\kappa\left(n_j^2 - 2l_1 n_j\right)\right) \cdot s_1. \tag{20}$$

Δn_{jk} is always smaller than the total volume height H. Examining the middle exponential term, it can be easily found that it always has a phase close to zero in the case that $\Delta l \ll \lambda\langle r\rangle/2H$ [see also (9)]. The expression then reduces to the correct result of a signal acquired from position $l_2 + \Delta l$

$$s_3^+ \simeq \sum_k \exp\left(-\kappa\left(n_k^2 - 2\left(l_2 + \Delta l\right) n_k\right)\right). \tag{21}$$

For nonvanishing baseline lengths Δl, the synthesized signals derived by the proposed method are corrupted by the influence of the error term in (20). In practice, the usage of baselines up to half of the actual gap to be filled up is a necessity. But as long as the gap is below the Nyquist-criterion or only slightly violates it, the derived signals can still be considered as valid approximations of the correct signals.

REFERENCES

[1] J. C. Curlander and R. McDonough, *Synthetic Aperture Radar—Systems and Signal Processing*. New York: Wiley.

[2] H. Floyd and A. J. Lewis, *Principles and Applications of Imaging Radar—Manual of Remote Sensing*. New York: Wiley, 1998, vol. 2.

[3] S. R. Cloude and E. Pottier, "A review of target decomposition theorems in radar polarimetry," *IEEE Trans. Geosci. Remote Sensing*, vol. 34, pp. 498–518, Mar. 1996.

[4] S. R. Cloude and K. P. Papathanassiou, "Polarimetric SAR interferometry," *IEEE Trans. Geosci. Remote Sensing*, vol. 36, pp. 1551–1565, Sept. 1998.

[5] K. P. Papathanassiou, "Polarimetric SAR interferometry," Ph.D. dissertation, Univ. Technol., Graz, Austria, 1999.

[6] K. P. Papathanassiou and S. R. Cloude, "Phase decomposition in polarimetric SAR interferometry," in *Proc. IGARSS'98*, Seattle, WA, 1998, pp. 2184–2186.

[7] R. A. Brooks and G. DiChiro, "Principles of computer-assisted tomography in radiographic and radioisotopic imaging," *Phys. Med. Biol.*, vol. 21, pp. 689–732, 1976.

[8] R. M. Mersereau and A. V. Oppenheim, "Digital reconstruction of multidimensional signals from their projections," in *Proc. IEEE*, vol. 62, Oct. 1974, pp. 1319–1338.

[9] D. C. Munson, J. D. O'Brien, and W. K. Jenkins, "A tomographic formulation of spotlight-mode synthetic aperture radar," in *Proc. IEEE*, vol. 71, Aug. 1983, pp. 917–925.

[10] D. C. Munson and J. L. C. Sanz, "Image reconstruction from frequency-offset Fourier data," *Proc. IEEE*, vol. 72, pp. 661–669, June 1984.

[11] M. D. Desai and W. K. Jenkins, "Convolution backprojection image reconstruction for spotlight mode synthetic aperture radar," *IEEE Trans. Geosci. Remote Sensing*, vol. 30, pp. 505–515, July 1992.

[12] R. K. Raney, H. Runge, R. Bamler, I. Cumming, and F. Wong, "Precision SAR processing without interpolation for range cell migration correction," *IEEE Trans. Geosci. Remote Sensing*, vol. 32, pp. 786–799, July 1994.

[13] R. Bamler, "A comparison of range-doppler and wavenumber domain SAR focusing algorithms," *IEEE Trans. Geosci. Remote Sensing*, vol. 30, pp. 706–713, July 1992.

[14] A. Moreira, J. Mittermayer, and R. Scheiber, "Extended chirp scaling algorithm for air- and spaceborne SAR data processing in stripmap and ScanSAR imaging modes," *IEEE Trans. Geosci. Remote Sensing*, vol. 34, pp. 1123–1136, Sept. 1996.

[15] J. Mittermayer, A. Moreira, and O. Loffeld, "The frequency scaling algorithm for spotlight SAR data processing," *IEEE Trans. Geosci. Remote Sensing*, vol. 37, Sept. 1999.

[16] F. Rocca, C. Prati, and A. Monti Guarnieri, "New algorithms for processing of SAR data," Eur. Space Center Contract Rep., Ispra, Italy, ESRIN Contract no. 7998/88/F/FL(SC), 1989.

[17] C. Cafforio, C. Prati, and F. Rocca, "SAR data focusing using seismic migration techniques," *IEEE Trans. Aerosp. Electron. Syst.*, vol. 27, pp. 194–207, Feb. 1991.

[18] W. G. Carrara, R. S. Goodman, and R. M. Majewski, *Spotlight Synthetic Aperture Radar*. Norwood, MA: Artech House.

[19] A. Ishimaru, T. Z. Chan, and Y. Kuga, "An imaging technique using confocal circular synthetic aperture radar," *IEEE Trans. Geosci. Remote Sensing*, vol. 36, pp. 1524–1530, Sept. 1998.

[20] J. Homer, I. D Longstaff, and G. Callaghan, "High resolution 3-D SAR via multi-baseline interferometry," in *Proc. IGARSS'96*, Lincoln, NE, 1996, pp. 796–798.

[21] C. K. Chan and N. H. Farhat, "Frequency swept tomographic imaging of three-dimensional perfectly conducting objects," *IEEE Trans. Antennas Propagat.*, vol. AP-29, pp. 312–319, Feb. 1981.

[22] N. H. Farhat, C. L. Werner, and T. H. Chu, "Prospects for three-dimensional projective and tomographic imaging radar networks," *Radio Sci.*, vol. 19, no. 5, pp. 1347–1355, 1984.

[23] P. Pasquali, C. Prati, F. Rocca, M. Seymour, J. Fortuny, E. Ohlmer, and A. J. Sieber, "A 3-D SAR experiment with EMSL data," in *Proc. IGARSS'95*, Firenze, Italy, 1995, pp. 784–786.
[24] M. Byrd, A. J. Blanchard, and B. Krenek, "Use of confocal techniques in the generation of three dimensional images using conventional SAR," in *Poster presentation, IGARSS*, Lincoln, NE, May 1996, pp. 27–31.
[25] F. Gatelli, A. Monti-Guarnieri, F. Parizzi, P. Pasquali, C. Prati, and F. Rocca, "The wavenumber shift in SAR interferometry," *IEEE Trans. Geosci. Remote Sensing*, vol. 32, pp. 855–864, July 1994.
[26] Z. She, D. A. Gray, R. E. Bogner, and J. Homer, "Three-dimensional SAR imaging via multiple pass processing," in *Proc. GARSS'99*, Hamburg, Germany, 1999, pp. 2389–2391.
[27] R. Scheiber, A. Reigber, A. Ulbricht, K. P. Papathanassiou, R. Horn, S. Buckreuss, and A. Moreira, "Overview of interferometric data acquisition and processing modes of the experimental airborne SAR system of DLR," in *Proc. IGARSS'99*, Hamburg, Germany, 1999, pp. 35–38.
[28] K. Tomiyasu, "Conceptual performance of a sattelite borne, wide swath synthetic aperture radar," *IEEE Trans. Geosci. Remote Sensing*, vol. GE-19, pp. 108–116, Mar. 1981.
[29] M. Sack *et al.*, "Application of efficient linear FM matched filtering algorithms to synthetic aperture radar processing," *Proc. Inst. Elect. Eng.*, pt. F, vol. 132, no. 1, pp. 45–57, 1985.
[30] S. M. Kay and S. L. Marple, "Spectrum analysis—A modern perspective," *Proc. IEEE*, vol. 69, pp. 1380–1419, Nov. 1981.
[31] A. Moreira and Y. Huang, "Airborne SAR processing of highly squinted data using a chirp scaling approach with integrated motion compensation," *IEEE Trans. Geosci. Remote Sensing*, vol. 32, pp. 1029–1040, Sept. 1994.
[32] J. J. van Zyl, H. Zebker, and C. Elachi, "Imaging radar polarization signatures: Theory and application," *Radio Sci.*, vol. 22, no. 4, pp. 529–543, 1987.
[33] G. Smith and L. M. H. Ulander, "A model relating VHF-band backscatter to forest stem volume," *IEEE Trans. Geosci. Remote Sensing*, vol. 38, Mar. 2000.
[34] A. Ulbricht, "Flugzeuggetragenene repeat-pass interferometrie mit dem E-SAR," Ludwig-Maximilian Univ. München, München, Germany, 2000.
[35] W. Xu *et al.*, "Phase unwrapping of SAR interferograms with multi-frequency or multi-baseline," in *Proc. IGARSS'94*, Pasadena, CA, 1994, pp. 730–732.
[36] D. Massonet, H. Vadon, and M. Rossi, "Reduction of the need for phase unwrapping in radar interferometry," *IEEE Trans. Geosci. Remote Sensing*, vol. 34, pp. 489–497, Mar. 1996.

Andreas Reigber was born in 1970 in Munich, Germany. He received the Diploma degree in physics from the University of Konstanz, Konstanz, Germany, in 1997. He is currently pursuing the Ph.D. degree at the University of Stuttgart, Stuttgart, Germany, in the field of synthetic aperture radar (SAR) tomography.

Since 1996, he has been with the Institute for Radio Frequency Technology, German Aerospace Center (DLR), Oberpfaffenhofen, Germany. In 1997, he was involved with ERS-1 SAR interferometry and differential interferometry and developed a robust SAR phase unwrapping algorithm based on the fusion of local and global methods. In 1998 he participated in a multisensor airborne campaign over Mount Etna, Italy. He has also developed a high precision SAR processor including a two step motion compensation for multipass airborne SAR interferometry and tomography. His main research interests are SAR interferometric processing, airborne repeat-pass interferometry, SAR polarimetry, polarimetric SAR interferometry, and SAR tomography.

Alberto Moreira (M'92–S'96) was born in São José dos Campos, Brazil, in 1962. He received the B.S.E.E. and the M.S.E.E. degrees, in 1984 and 1986, respectively, from the Aeronautical Technological Institute (ITA), Brazil, and the Eng. Dr. degree ("mit Auszeichung" - Hons.) from the Technical University of Münich, Münich, Germany, in 1993.

From 1985 to 1986, he was with ITA as a Research Assistant and Consultant. In 1987, he received a four-year scholarship from DAAD, Germany, to work toward his Ph.D. at the German Aerospace Center (DLR - Institut für Hochfrequenztechnik) in the area of SAR signal processing. From 1992 to 1995, he was the Head of the Signal Processing Group with DLR and was responsible for the development of a high resolution real-time airborne SAR processor. As Chief Scientist and Engineer with DLR since 1996, he manages the DLR SAR Technology Department. Under his leadership, the DLR airborne SAR system has been upgraded to operate in innovative imaging modes like polarimetric SAR interferometry and polarimetric SAR tomography. He is currently serving as a member of the Administrative Committe of the Geoscience and Remote Sensing Society.

Dr. Moreira was the recipient of the DLR Science Award in 1995. In 1996, he and his colleagues received the IEEE 1996 Transactions Prize Paper Award for the development of the so-called "Extended Chirp Scaling Algorithm." In 1999, he received the IEEE AESS Fred Nathanson Memorial Award to the Young Radar Engineer of the Year. His professional interests and research areas encompass SAR end-to-end system design and analysis, SAR signal processing and interferometry, innovative radar techniques, and expert systems for data fusion and classification.